Insight into cathode surface to boost the performance of solid-state batteries

Sixu Deng [a,1], Qian Sun [a,1], Minsi Li [a], Keegan Adair [a], Chuang Yu [a], Junjie Li [a], Weihan Li [a], Jiamin Fu [a], Xia Li [a], Ruying Li [a], Yongfeng Hu [b], Ning Chen [b], Huan Huang [d], Li Zhang [c], Shangqian Zhao [c], Shigang Lu [c], Xueliang Sun [a,*]

[a] *Department of Mechanical and Materials Engineering, University of Western Ontario, London, Ontario N6A 5B9, Canada*
[b] *Canadian Light Source, 44 Innovation Boulevard, Saskatoon, Saskatchewan S7N 2V3, Canada*
[c] *China Automotive Battery Research Institute Co. Ltd, Fifth Floor, No. 43, Mining Building, North Sanhuan Middle Road, Beijing 100088, China*
[d] *Glabat Solid-State Battery Inc., 700 Collip Circle, London, Ontario N6G 4X8, Canada*

A B S T R A C T

Cathode interface instability is a significant obstacle for the practical application of sulfide-based all-solid-state lithium-ion batteries (ASSLIBs). However, the origin of cathode interface degradation is lack of comprehensive understanding. In this paper, X-ray characterizations combined with electrochemical analysis are adopted to investigate the underlying degradation mechanism at cathode interface. The results indicate that residual lithium compounds on the surface of Ni-rich $LiNi_{0.8}Mn_{0.1}Co_{0.1}O_2$ (NMC811) are the main reason that triggering the oxidation of sulfide solid-state electrolytes (SSEs), therefore inducing severe side-reactions at cathode interface and structural degradation of NMC811. The degradation of the cathode interface can be significantly suppressed when the cathode surface is cleaned. As a result, the surface cleaned NMC811 without coating demonstrates significantly improved electrochemical performance in both $Li_{5.5}PS_{4.5}Cl_{1.5}$ (LPSCl) and $Li_{10}GeP_2S_{12}$ (LGPS) based ASSLIBs, proving the universal application of this strategy.

1. Introduction

The use of inflammable solid-state electrolytes (SSEs) makes all-solid-state lithium-ion batteries (ASSLIBs) as promising energy storage devices that can meet the safety requirements of electric vehicles [1–3]. Among the developed SSEs, sulfide-based electrolytes, such as Li_6PS_5Cl (LPSCl) and $Li_{10}GeP_2S_{12}$ (LGPS), have demonstrated high room-temperature lithium-ion conductivities (10^{-2} to 10^{-3} S cm^{-1}), which are comparable with liquid electrolytes [4–6]. Meanwhile, sulfide-based ASSLIBs have great potential to reach competitive energy densities of over 350 Wh kg^{-1} when coupled with high-energy cathodes and lithium metal anodes [7,8]. Therefore, selection of suitable high-performance cathode materials is critical towards achieving the energy density target. In conventional lithium-ion batteries, Ni-rich layered oxide cathodes, $LiNi_xMn_yCo_{1-x-y}O_2$ (NMC), have become mainstream because of their high specific capacities. For example, a specific capacity of roughly 200 mAh g^{-1} can be reversibly accessed from $LiNi_{0.8}Mn_{0.1}Co_{0.1}O_2$ (NMC811) [9,10]. However, the performance of

Ni-rich NMC cathodes in sulfide-based ASSLIBs is still limited by the undesired chemical/electrochemical reactions.

The most significant challenge of Ni-rich NMC cathodes in sulfide-based ASSLIBs is the poor interfacial compatibility. The severe side-reactions between Ni-rich NMC cathodes and sulfide SSEs trigger the oxidative decomposition of sulfide SSEs, in particular at high potentials during charging [11]. As a result, the formation of an unfavorable cathode electrolyte interface (CEI) and degradation of the structure at cathode surface lead to rapid capacity fading, low initial capacity, and poor Columbic efficiency [12,13]. Although a prevailing coating strategy combined with various coating materials is widely applied for the cathode surface modification in sulfide-based ASSLIBs [14–19], the underlying degradation mechanism of the cathode interface, especially the origin of the oxidation of sulfide SSEs, is still not clear. The reasonable speculation is that the oxidation of sulfide SSEs is derived from oxygen-containing species in the cathode [20]. On the one hand, oxygen release from the cathode structure at high charge voltage is one possible reason [21,22]. On the other hand, residual lithium compounds, such as Li_2CO_3 and LiOH, on the surface of Ni-rich NMC cathodes are considered as the possible oxygen sources that result in the reaction with sulfide SSEs [23]. Therefore, two questions arise here: (1) what is the main origin of

---

reaction with sulfide SSEs, cathodes themselves or residual lithium compounds? (2) Is it possible to circumvent the side-reactions by eliminate the origin of oxygen sources?

To answer aforementioned questions, in this study, we adopt the comprehensive electrochemical testing and X-ray characterizations to investigate the underlying degradation mechanism of pristine NMC811 with residual lithium compounds in sulfide-based solid-state batteries (SSBs). The results suggest that the surface impurities of the cathodes, instead of cathode particles themselves, are the main reason that accelerating the oxidation of sulfide SSEs, therefore leading to the structural degradation of NMC811 and fast capacity decay. Promisingly, the removal of the residual lithium compounds effectively alleviates the severe side-reactions between NMC811 and sulfide SSEs, therefore enhancing the interfacial stability and resulting in clearly improved cycling stability with the higher initial capacity and Columbic efficiency in different sulfide-based SSBs with $Li_{5.5}PS_{4.5}Cl_{1.5}$ (LPSCl) and LGPS SSEs. This study reveals the origin of side-reactions of cathode interface in sulfide-based SSE systems, effectively promoting the potential commercialization of high-performance ASSLIBs.

2. Material and methods

2.1. Preparation of cathodes and sulfide solid-state electrolytes

The commercial $LiNi_{0.8}Mn_{0.1}Co_{0.1}O_2$ (NMC811) and $LiNi_{0.5}Mn_{0.3}Co_{0.2}O_2$ (NMC532) are obtained from China Automotive Battery Research Institute Co., Ltd, China. For the surface modification, both NMC811 and NMC532 powders were heated at 730 °C for 1 h under the continued O_2 flow, which is followed by the reference [24]. The ALD $LiNbO_x$ coating process was reported in our previous studies [25]. Prior to use, the material was stored in a glovebox under Ar. For sulfide solid-state electrolytes (SSEs), $Li_{5.5}PS_{4.5}Cl_{1.5}$ (LPSCl) is synthesized following our previous study [6], while $Li_{10}GeP_2S_{12}$ (LGPS, 99.95%) is commercial electrolyte, purchasing from MSE supplies, LLC, United States.

2.2. Assembly of the tested batteries and electrochemical testing

In order to investigate the electrochemical performance, the sandwiched model cells were fabricated by using the as-prepared NMC811 cathodes combining with LPSCl or LGPS as SSE layer and indium foil (99.99%, Φ10 mm, thickness 0.1 mm) as anode. The detailed fabrication process is shown as follow. Firstly, 60 mg LPSCl or LGPS was pressed at 2 ton with 10 mm diameter to form a pellet. After that, 7 mg NMC811 power was mixed well with 3 mg LPSCl or LGPS, and then uniformly spread onto the surface of SSE layer and pressed under 3 tons of pressure to form a two-layer pellet. Finally, a piece of indium foil with the same 10 mm diameter was put onto the other side of the SSE layer with a copper foil and pressed at 0.5 tons of pressure. The three-layered pellet was pressed between two stainless-steel rods as current collectors at the both positive and negative sides. When Li compounds were added in the cathode composites, 1 wt%, 5 wt%, and 10 wt% Li_2CO_3 + LiOH were mixed with treated NMC811 and LPSCl to form the cathode layer. The weight ratio of Li_2CO_3: LiOH was 1: 1. The assembly of NMC532 model cells is same as the process of NMC811. All the processes were performed in an argon-filled glove box. The galvanostatic charge-discharge characteristics were tested in the range of 2.1–3.8 V vs. Li^+/Li-In, corresponding to 2.7–4.4 V vs. Li^+/Li by using a multichannel battery tester (LAND CT-2001A, Wuhan Rambo Testing Equipment Co., Ltd., China). Electrochemical impedance spectroscopy (EIS) was performed on the versatile multichannel potentiostat 3/Z (VMP3) by applying an AC voltage of 10 mV amplitude in the 7000 kHz to 1000 mHz frequency range. For galvanostatic intermittent titration technique (GITT) measurements, the cells were charged and discharged with 0.05 C for 10 min and rest for 1 h. According to the GITT theoretical analysis, Li^+ diffusion coefficient

can be calculated by following equation:

$$D_{Li} = \frac{4}{\pi\tau}\left(\frac{m_B V_m}{M_B S}\right)^2 \left(\frac{\Delta E_s}{\Delta E_\tau}\right)^2 \left(\tau \ll L^2/D\right) \qquad (1)$$

Where D is chemical diffusion coefficient; S is interfacial contact area between NMC811 and sulfide SSEs in our case, the specific area of NMC811 is 0.55 m^2 g^{-1}; τ is pulse duration (600 s in our case), ΔE_s is the steady-state voltage change; ΔE_t is the transient voltage change; m_B is the mass of the LCO in the cathode composite (7 mg); M_B is the molecular weight of NMC811 (97.28 g. mol^{-1}); V_m is the molar volume of NMC811 (20.33 cm^3 mol^{-1})[26].

2.3. Characterizations

The crystalline structure of the pristine and treated NMC811 were conducted on a Bruker D8 Advance Diffractometer (Cu-Ka source, 40 kV, 40 mA). The morphology and microstructure of the pristine and treated NMC811 were characterized using field emission scanning electron microscopy (FESEM, Hitachi S4800). The $LiNbO_x$ coating layer on the surface of NMC811 was observed by a high-resolution transmission electron microscopy (HRTEM, JEOL 2010F). For the thermal gravimetric analysis (TGA) testing, the data were acquired using a TA instrument (SDT Q600) in a nitrogen atmosphere at a heating rate of 2 °C min^{-1}. X-ray photoelectron spectroscopy (XPS) testing were measured with a monochromatic Al $K\alpha$ source (1486.6 eV) in a Kratos AXIS Nova Spectrometer. The Ar filled glovebox was connected with the XPS machine to avoid the exposure of air. All synchrotron X-ray studies were carried out at the Canadian Light Source (CLS). X-ray absorption fine structure (EXAFS) data were collected at Hard X-ray Micro Analysis (HXMA) beamline. Ni K-edge spectra were collected in fluorescence mode using Si(220) crystals. Co and Mn K-edge spectra were also collected in fluorescence mode but using Si(111) crystals. S, P, Cl, Ni, Co, and Mn K-edge X-ray absorption near edge structure (XANES) spectra were collected in fluorescence mode using Si(111) crystals at Soft X-ray Microcharacterization Beamline (SXRMB). To avoid air exposure, the samples were firstly covered with Kapton tape for HXMA test and Mylar film for SXRMB test in glovebox under Ar, and then transferred to the corresponding beamlines for further measurements. O K-edge XANES spectra were collected in both total electron yield and fluorescence mode at Spherical Grating Monochromer (SGM) beamline equipped with a 45 mm planar undulator.

3. Results and discussion

To investigate the effect of impurities on the surface of NMC811 cathode, a high temperature treatment process at 730 °C for 1 h under continuous O_2 flow is adopted to remove the residual lithium compounds on the surface of NMC811 particles (Fig. 1a). To identify if changes in the crystal structure of NMC811 occur during the surface modification, X-ray diffraction (XRD) measurements were first conducted for both pristine and treated NMC811. The results show good retention of the NMC811 crystallinity without noticeable impurity phase caused by the surface modification (Fig. 1b). Furthermore, the bulk structure of NMC811 is investigated by X-ray absorption spectroscopy (XAS), in which both pristine and treated NMC811 show nearly identical features in the Ni, Co, Mn K-edge X-ray absorption near edge structure (XANES) and extended X-ray absorption fine structure (EXAFS) spectra as shown in Figs. 1c-h, suggesting that no measurable structure evolution of NMC811 resulted from the surface-cleaning procedure.

In addition, the surface-clean effect is also investigated by different characterizations. The C 1 s and O 1 s X-ray photoelectron spectroscopy (XPS) spectra are displayed in Fig. 1i and j, respectively, to analyze the components on the surface of both pristine and treated NMC811. In the C 1 s XPS spectra, in addition to the adventitious carbon peak at 284.4 eV from internal calibrator, another carbon peak at 289.3 eV is attributed
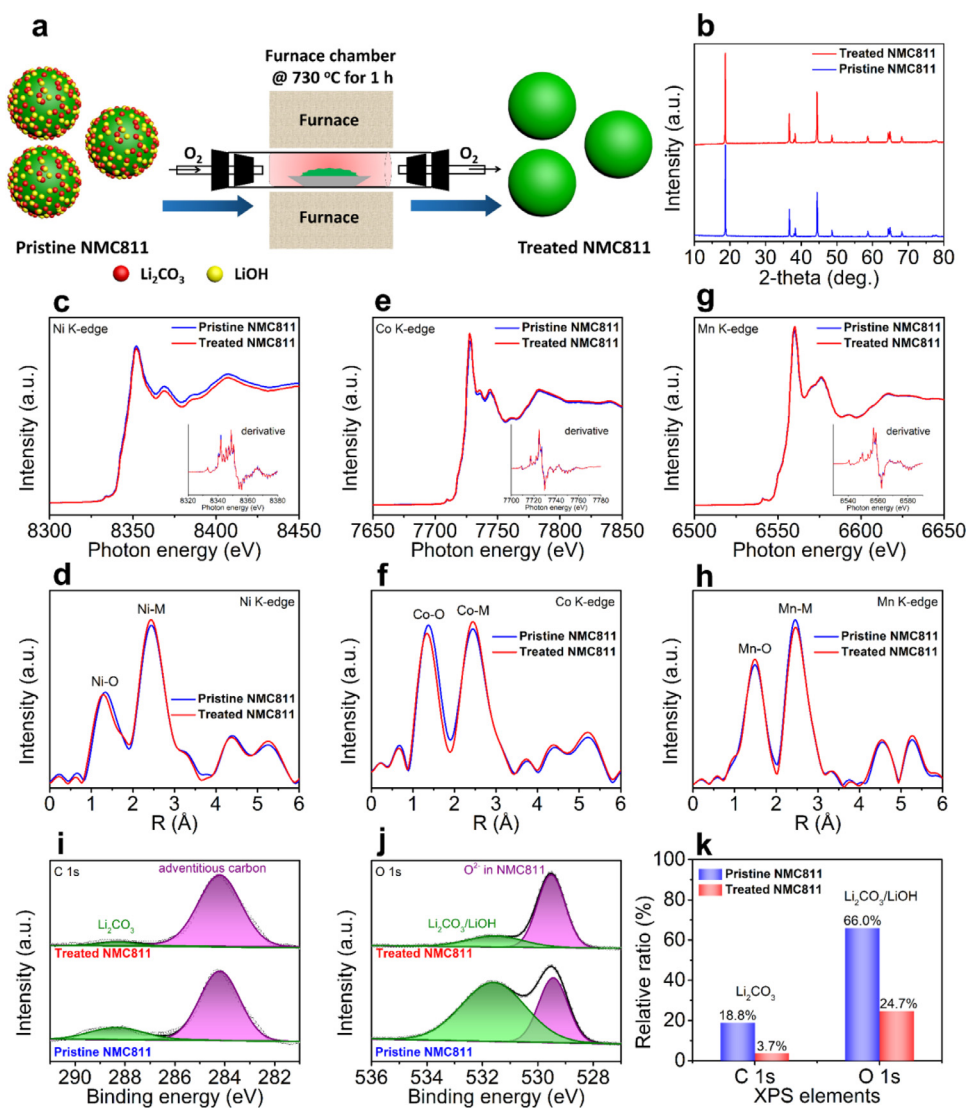
Fig. 1. Structural and morphological characterizations of the Ni-rich NMC cathode before and after cleaning the surface. (a) Schematic illustration of the surface treatment process for NMC811. (b) XRD patterns of the pristine and treated NMC811. (c-h) Ni, Co, and Mn K-edge XANES and Fourier transformed R space EXAFS spectra: (c-d) Ni K-edge spectra, (e-f) Co K-edge spectra, and (g-h) Mn K-edge spectra. (i-k) XPS spectra of the pristine and treated NMC811: (i) C 1s, (j) O 1s, and (j) the corresponding relative ratio of Li_2CO_3/LiOH in XPS.

to Li_2CO_3 [27,28]. After normalizing the peak intensities to the adventitious carbon, the pristine NMC811 shows relatively higher amounts of residual Li_2CO_3 than that of the treated NMC811. O 1 s spectra also comprises of two peaks, corresponding to the peak of Li_2CO_3/LiOH at 531.5 eV and the peak of O^{2-} ions in NMC811 at 829.5 eV [29]. The relative ratio of Li_2CO_3/LiOH peaks of both pristine and treated NMC811 is shown in Fig. 1k. The treated NMC811 shows obvious reduce amounts of residual lithium compounds comparing to the pristine NMC811. Moreover, O K-edge XANES spectra of the pristine and treated NMC811 are demonstrated in Figure S1. The peak at 534 eV is assigned to the oxygen in Li_2CO_3/LiOH [30,31], which is suppressed in the treated NMC811 comparing to the pristine NMC811. The morphologies of the pristine and treated NMC811 are characterized using scanning electron microscopy (SEM) as shown in Figure S2. The pristine NMC811 particles show folds on the rough surfaces, while the treated NMC811 particles present very smooth surfaces. From the thermal gravimetric analysis (TGA) profiles (Figure S3), the more obvious weight loss started from 730 °C can be observed in the pristine NMC811. Therefore, combining the comprehensive characterizations, residual lithium compounds on the surface of NMC811 are successfully removed by the surface modification procedure.

To investigate the universal effect of the surface impurities on the cathode interface, two promising sulfide SSEs, LPSCl and LGPS, are employed for electrochemical characterizations. LPSCl-based SSBs are first tested and the configuration of the designed model cell is shown in Fig. 2a. A mixture of NMC811 and LPSCl is used as the cathode combined with LPSCl as the electrolyte layer and indium foil as the anode. Fig. 2b shows a comparison of the initial charge-discharge curves between the pristine and treated NMC811 at 0.05 C. The initial charge and discharge capacities of the pristine NMC811 are 162.3 and 111.1 mAh g^{-1}, respectively. In contrast, the treated NMC811 presents higher charge and discharge capacities (206.2 and 156.8 mAh g^{-1}, respectively) with reduced irreversible capacity loss. The corresponding differential capacity profiles as a function of voltage indicate reduced polarization during the redox reactions in the treated NMC811 (Figure S4). Furthermore, the treated NMC811 demonstrates higher Coulombic efficiency (76.0% vs. 68.4%) and average discharge voltage (3.79 V vs. 3.77 V) than that of the pristine NMC811 as shown in Fig. 2c.

To gain further insight into the lithium-ion diffusion kinetics of NMC811 in LPSCl-based SSBs, the galvanostatic intermittent titration technique (GITT) was conducted for both pristine and treated NMC811 during the initial charge-discharge process (Fig. 2d). The corresponding polarization plots and lithium-ion diffusion coefficients (D_{Li}) are demonstrated in Fig. 2e and f, respectively. It is apparent that the treated NMC811 presents higher charge and discharge capacities with greatly reduced polarization potential especially during the discharging process. Meanwhile, the D_{Li} of NMC811 during the charge and discharge processes are also calculated based on the GITT curves by the Eq. (1)[26]
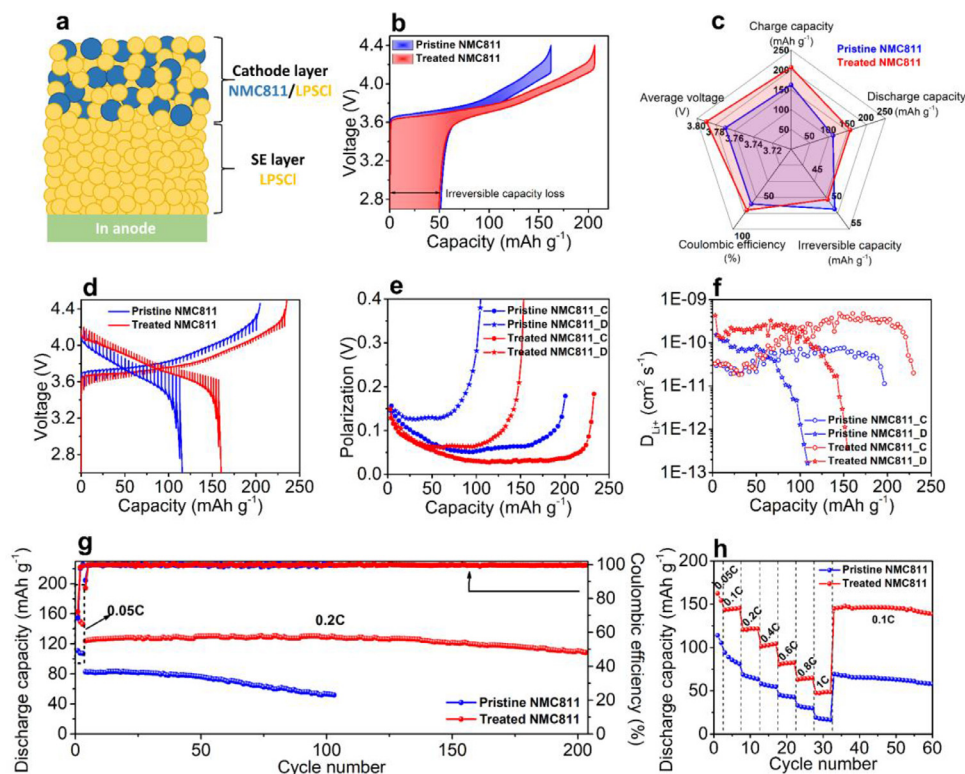
Fig. 2. Comparison of the electrochemical performance of pristine and treated NMC811 in LPSCl SSBs. (a) Schematic illustration of the designed model cell, (b) charge-discharge curves of the first cycle at 0.05 C, (c) the corresponding performance parameters collected from charge-discharge curves, (d) GITT curves during the charge-discharge process, (e) the corresponding polarization plots and (f) lithium-ion diffusion coefficients, (g) cycling stability, and (h) rate capability.

as follows:

$$D_{Li} = \frac{4}{\pi\tau}\left(\frac{m_B V_m}{M_B S}\right)^2\left(\frac{\Delta E_s}{\Delta E_\tau}\right)^2 \quad (\tau \ll L^2/D) \tag{1a}$$

During the delithiation process, D_{Li} increases with continued lithium-ion removal from the layered structure until the highest value is achieved, which is followed by a gradual decrease. During the lithiation process, D_{Li} retains a value within the same order of magnitude at the beginning of discharge, and then decreases dramatically by two orders of magnitude at the end of discharge. Considering that the diffusion kinetics is assumed to be the same in the bulk of the NMC811 particles, the difference of the lithium-ion diffusion properties between the pristine and treated NMC811 is determined by the interfacial ionic conductivity. Although maintaining almost the same values at the beginning of charge, the treated NMC811 shows one order of magnitude higher D_{Li} of 10^{-10} cm^2 s^{-1} than that of the pristine NMC 811 (10^{-11} cm^2 s^{-1}) with the deepening of the charge process. During the entire discharge process, D_{Li} of the treated NMC811 is higher than that of the pristine NMC811. Combined with the findings from the charge-discharge and GITT results, the treated NMC811 demonstrates improved electrochemical performance, suggesting that the treated surface of NMC811 is beneficial towards the suppression of side-reactions with LPSCl SSE, therefore helping the NMC811 to obtain higher lithium-ion diffusion kinetics during the initial charge-discharge process.

Cycling stability testing was also conducted to evaluate the effect of the surface impurities of NMC811 during long-term cycling. The treated NMC811 demonstrated an initial discharge capacity of 123.9 mAh g^{-1} with a capacity retention of 87.7% after 200 cycles when the current density switches to 0.2 C (Fig. 2g). In contrast, the pristine NMC811 delivers a low initial discharge capacity of 82.7 mAh g^{-1} at 0.2 C with a poor capacity retention of 62.9% only after 100 cycles. The electrochemical impedance spectroscopy (EIS) plots of both pristine and treated NMC811 indicate the reduced interfacial resistance after cycling by cleaning the cathode surface (Figure S5). Moreover, to exclude the effect of NMC811 themselves, the different contents of Li compounds were mixed with the treated NMC811 and LPSCl in the cathode com-

posites. The electrochemical performance shown in Figure S6 indicates that the Li compounds as impurities in cathode composites deteriorate the performance of sulfide-based SSBs. The rate capability of the pristine and treated NMC811 also shows considerable differences as shown in Fig. 2h. The rate capacities of the pristine NMC811 dramatically decay with an increase of current density. In contrast, the treated NMC811 demonstrates improved rate capacities at each current density. The discharge capacity of the treated NMC811 is still higher than 45 mAh g^{-1} at 1 C, which is over 2.5 times that of the pristine NMC811. The aforementioned electrochemical performance of NMC811 in LPSCl-based SSBs indicates that the cleaned surface helps Ni-rich NMC cathodes to achieve higher discharge capacity, greater cycling stability, and rate capability with enhanced D_{Li} and reduced polarization. Even comparing to the prevailing ALD LiNbO$_x$ coating, the treated NMC811 also demonstrated a comparable long-term cycling stability (Figures S7–8). Furthermore, the effect of surface cleaning is also demonstrated in NMC532 cathodes (Figure S9). The treated NMC532 shows much improved capacity and cycling stability, proving the universality of the surface-cleaning strategy.

In order to investigate the interfacial stability between LPSCl and NMC811 with and without surface impurities, XPS and XANES measurements were performed. Figure S10 and Fig. 3a-b show the S 2p XPS spectra of the LPSCl SSEs collected from the pristine LPSCl, cycled pristine electrode (denoted as C-Pristine), and cycled treated electrode (denoted as C-Treated), respectively. The C-Pristine electrode shows higher relative content of SO$_3^{2-}$ than the C-Treated electrode. Moreover, the further oxidized products of LPSCl, SO$_4^{2-}$, can be observed in the C-Pristine electrode but are essentially absent in the C-Treated electrode. Fig. 3c shows the S K-edge XANES spectra of the LPSCl SSEs collected from the C-Pristine and C-Treated with a pristine LPSCl as reference, which are in agreement with the XPS results. A new peak at 2481.9 eV in the C-Pristine electrode increases noticeably compared to that of the pristine LPSCl, indicating the formation of sulfate species as the by-product in LPSCl during cycling [32,33]. This result is highly consistent with our previous studies on the use of NMC811/LGPS SSBs with and without car-
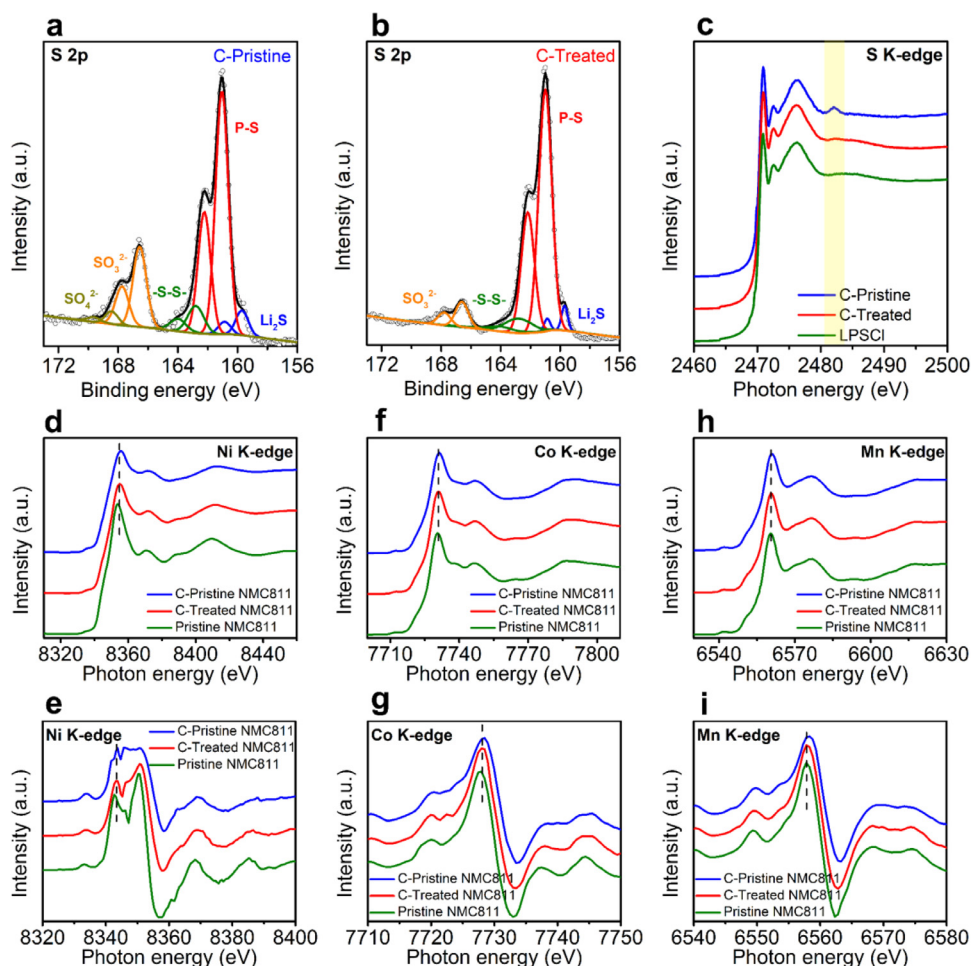
Fig. 3. Understanding the chemical interactions between NMC811 and LPSCl during electrochemical cycling in LPSCl SSBs. S 2p XPS spectra of the (a) cycled pristine electrode (C-Pristine) and (b) cycled treated electrode (C-Treated), (c) S K-edge XANES spectra of LPSCl in the C-Pristine and C-Treated cells with pristine LPSCl as a reference. (d-i) Ni, Co, and Mn K-edge XANES spectra of the C-Pristine and C-Treated NMC811 with pristine NMC811 as a reference: (d) Ni K-edge and (e) the corresponding first derivative spectra, (f) Co K-edge and (g) the corresponding first derivative spectra, (h) Mn K-edge and (i) the corresponding first derivative spectra.

bon additives [17,34]. Our previous studies demonstrated that the formation of sulfate species can be effectively suppressed by surface coating of cathode with either inorganic Li_3PO_4 or PEDOT polymer. Therefore, we proposed that the formed sulfate was derived from the oxygen participation from the NMC811 bulk structure, which could be alleviated by the construction of interfacial layer on the surface of NMC811. Interestingly, in the current study, the sulfate species are significantly suppressed in the C-treated electrode without coating protection. Considering the only difference between the C-Pristine and C-Treated electrodes is the treated surface, the findings suggest that the formation of sulfate is mainly attributed to the oxygen participation from residual lithium compounds on the surface of NMC811. Different from the S XPS results, the oxidation of P is obviously alleviated in the C-Pristine electrode as shown in Figure S11, indicating that the side-reactions between residual lithium compounds and LPSCl mainly lead to the oxidation of S rather than P in LPSCl. Impressively, removing residual lithium compounds from the cathode surface significantly suppresses the oxidation of LPSCl, therefore boosting the electrochemical performance.

The transition metal K-edge XANES spectra (TMs, including Ni, Co, and Mn) are presented in Fig. 3d-i to better understand the structural evolution of the layered NMC811 during cycling. It should be mentioned that both pristine and treated NMC811 were tested after being fully discharged to 2.7 V vs. Li$^+$/Li. Generally, the oxidation state of the TMs correspond to the threshold energy position of the K-edge XANES peaks, while the shape of the peaks is indicative of the TMs local structural environment [35–37]. The 2 eV peak energy shift for the Ni K-edge can be observed in the spectrum for the C-Pristine electrode (Fig. 3d), indicating the oxidation of Ni after cycling. In contrast, the C-Treated NMC811 demonstrates less change toward higher energy in the Ni K-edge posi-

tion after cycling. Consistent with our previous studies, the oxidation of Ni after cycling suggests that a portion of the lithium ions were unable to intercalate back into the layered structure of the NMC811 cathodes because of the formation of a cathode electrolyte interface (CEI) through severe side-reactions between residual lithium compounds and LPSCl [34]. As a result of the changes in the Ni environment, variations in peak shape and position of the Co and Mn K-edge XANES spectra are observed in C-Pristine NMC811, which are identified by the position shift of the first maximum in the derivative of the absorption curves, as shown in Fig. 3g and i. In contrast, the changes in the spectral features for the C-Treated NMC811 are less prominent. The shape variations of Co and Mn K-edge spectra indicate the structural evolution of NMC811 during cycling, which is induced from the side-reactions with LPSCl. Moreover, it can be concluded that the suppression of side-reactions aided by the cleaning of the NMC811 surface led to less structural change during cycling.

The electrochemical performance of the pristine and treated NMC811 is also demonstrated in LGPS-based SSBs and the configuration of the designed model is shown in Fig. 4a. The first charge-discharge profiles of the pristine and treated NMC811 at 0.05 C are demonstrated in Fig. 4b. The treated NMC811 shows a higher discharge capacity of 143.8 mAh g^{-1} with a Coulombic efficiency of 75.3%. However, the pristine NMC811 only delivered a discharge capacity of 105.3 mAh g^{-1} with a lower Coulombic efficiency of 67.5%. The corresponding differential capacity profiles as a function of voltage are shown in Fig. 4c to further reveal the different charge-discharge behaviors between the pristine and treated NMC811 in the initial cycle. It is clear that both the pristine and treated NMC811 show three pairs of redox peaks arising from the multiple phase transitions in NMC811 from hexagonal to
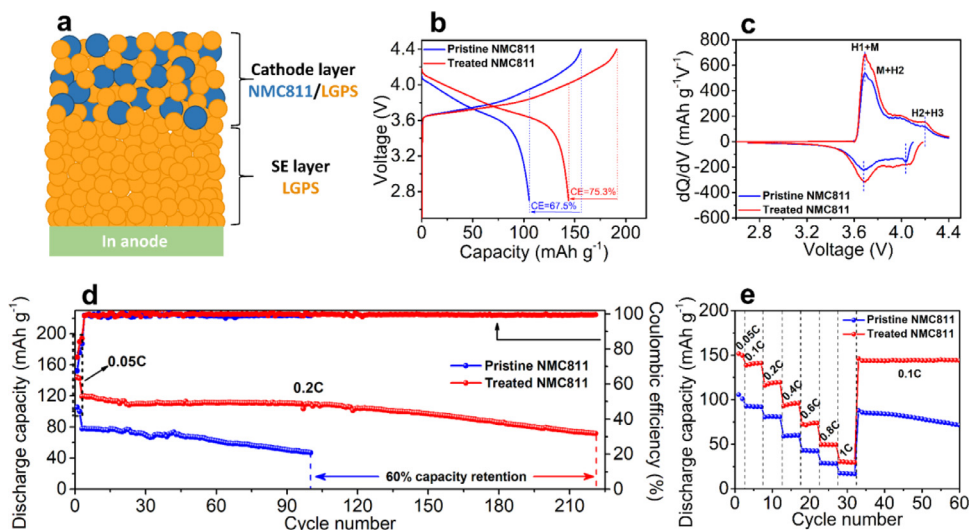
Fig. 4. Comparison of the electrochemical performance of pristine and treated NMC811 in LGPS SSBs. (a) Schematic illustration of the designed model cell, (b) charge-discharge curves of the first cycle at 0.05 C, (c) the corresponding differential capacity profiles, (d) cycling stability, and (e) rate capability.
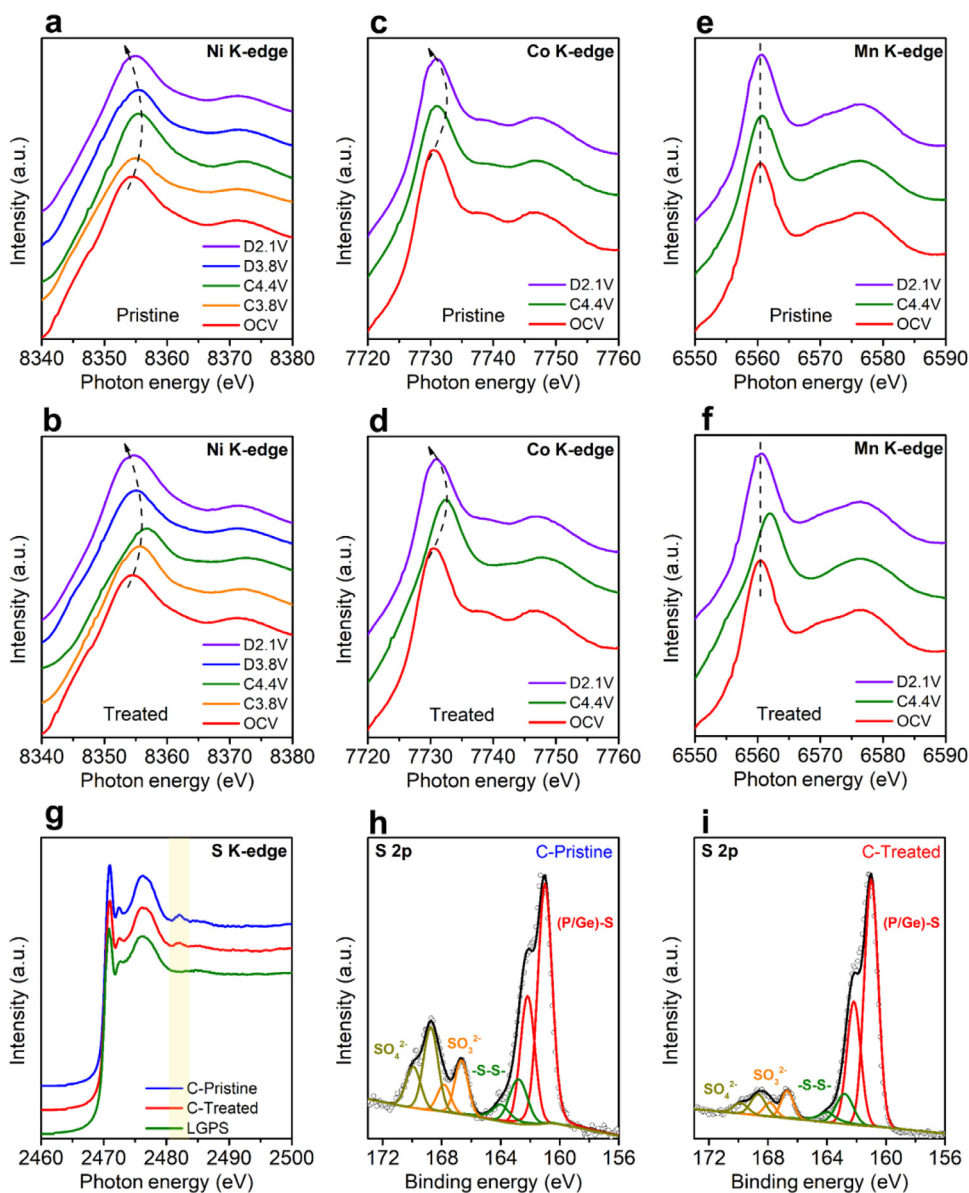

Fig. 5. Understanding the chemical interactions between NMC811 and LGPS during electrochemical cycling in LGPS SSBs. (a-f) Ni, Co, and Mn K-edge XANES spectra of the pristine and treated NMC811 at the different charge-discharge stages in the initial cycle: (a) Ni K-edge, (c) Co K-edge, and (e) Mn K-edge XANES spectra of the pristine NMC811; (b) Ni K-edge, (d) Co K-edge, and (f) Mn K-edge XANES spectra of the treated NMC811. (g) S K-edge XANES spectra of LGPS in the cycled pristine electrode (C-Pristine) and cycled treated electrode (C-Treated) cells with pristine LGPS as a reference. S 2p XPS spectra of the (h) C-Pristine and (i) C-Treated.

monoclinic (H1 to M), monoclinic to hexagonal (M to H2), and hexagonal to hexagonal (H2 to H3) during the delithiation-lithiation process [38,39]. The treated NMC811 demonstrates smaller voltage intervals between the pairs of anodic-cathodic peaks and higher peak intensities than that of the pristine NMC811, indicating enhanced electrochemical reaction activity with reduced polarization induced by the cleaned surface of NMC811. This conclusion is also confirmed by the GITT results, which demonstrate lower polarization potentials and higher D_{Li} during the initial charge-discharge process in the treated NMC811 as shown in Figure S12.

The long cycling stability of both pristine and treated NMC811 is also demonstrated in Fig. 4d. The SSBs are first activated with a low current density of 0.05 C for two cycles before switching to a high current density of 0.2 C for long-term cycling. Initial discharge capacities of 143.8 mAh g^{-1} (0.05 C) and 119.4 mAh g^{-1} (0.2 C) are achieved by the treated NMC811, which are much higher than those of the pristine NMC811 with capacities of 105.3 mAh g^{-1} at 0.05 C and 77.9 mAh g^{-1} at 0.2 C, respectively. Furthermore, the treated NMC811 reveals obviously improved cycling stability with 60% capacity retention after 219 cycles, which is much higher than that of the pristine NMC811, which had a 60% capacity retention after only 98 cycles. The EIS results indicate that the increase of the interfacial resistance after cycling in the treated NMC811 is much slower than that of the pristine NMC811 as shown in Figure S13. The rate capability at the different current densities ranging from 0.05 C to 1 C is displayed in Fig. 4e. The treated NMC811 demonstrates higher rate capacities under each current density compared to the pristine NMC811. Meanwhile, the cycling stability is also enhanced when the current density returns to 0.1 C, which is attributed to the advantages of the cleaned surface of NMC811. The improved electrochemical performance in both LPSCl-based and LGPS-based SSBs show the strong competitiveness when comparing to the reported coating strategies. The sources of the data are listed in Table S1. This result indicates that cleaning the surface of Ni-rich NMC cathodes is a promising strategy to achieve high-performance Ni-rich NMC in sulfide-based SSBs.

The cathode interfacial stability was also investigated in LGPS-based SSBs. Both pristine and treated NMC811 were tested at five different charge and discharge states including open-circuit voltage, charging to 3.8 V and 4.4 V, as well as discharging to 3.8 V and 2.1 V, which are denoted as OCV, C3.8 V, C4.4 V, D3.8 V, and D2.1 V, respectively. TMs K-edge XANES spectra of both pristine and treated NMC811 are presented in Figs. 5a-f to evaluate the evolution of NMC811 at different charge-discharge states in the initial cycle. From the Ni K-edge XANES spectra in Fig. 5a and b, both pristine and treated NMC811 show a reversible peak shift after a charge-discharge cycle. However, the treated NMC811 demonstrates a shift toward higher energy at the end of the charging state (C4.4 V), indicating a deeper charge because of the smaller polarization than that of the pristine NMC811, as demonstrated in the initial charge-discharge curves (Fig. 4b). Meanwhile, the Co and Mn K-edge XANES spectra also demonstrate reversible peak shifts in both pristine and treated NMC811 during the initial charge-discharge process (Figures S14 and S15). Interestingly, compared to the pristine NMC811, the more obvious energy shift in the Co K-edge XANES spectrum of the treated NMC811 at C4.4 V demonstrates that the deeper charging also triggers a Co redox reaction in NMC811 (Fig. 5c-d) [30]. Furthermore, the shape variation in Mn K-edge XANES spectra of the treated NMC811 shown in Fig. 5f reveals a change in the local environment of Mn atoms because of the more obvious structural evolution during delithiation-lithiation process than that of the pristine NMC811 (Fig. 5e). In contrast, after long-term cycling, more obvious peak evolution in the TMs K-edge XANES spectra can be observed in the pristine NMC811 compared to that of the treated NMC811 (Figures S16–18), although the SSBs were fully discharged to 2.7 V vs. Li$^+$/Li, indicating the structural evolution of NMC811 is derived from the side-reactions with LGPS.

The corresponding S K-edge XANES spectra of LGPS at different charge and discharge states are presented in Figure S19. There is no no-

ticeable energy shift or new peaks observed in either pristine or treated electrodes during the initial charge-discharge process. However, as is the case for LPSCl, both the S K-edge XANES and S 2p XPS spectra of LGPS in the pristine electrode reveals an obvious sulfate peak after long-term cycling, which is suppressed in the treated electrode (Figs. 5g-i and Figure S20). This result indicates that the formation of sulfate generally accumulates with further charge-discharge cycling because of the continued side-reactions between residual lithium compounds and LGPS, which is obviously alleviated by the surface modification. Therefore, removing residual lithium compounds on the surface of Ni-rich NMC significantly suppresses the oxidation of sulfide SSEs, thus alleviating the side-reactions between Ni-rich NMC cathode and sulfide SSEs during electrochemical cycling. In addition to the oxidation of S, the by-products of LGPS also can be observed in the P 2p spectra of both C-Pristine and C-Treated electrodes after the long-term cycling (Figure S21), indicating the decomposition of LGPS at high voltage when coupled with NMC811 cathodes.

4. Conclusion

In conclusion, the comprehensive electrochemical analyses and X-ray characterizations are adopted to investigate the origin of cathode interface degradation in sulfide-based ASSLIBs. The electrochemical results indicate that eliminating residual lithium impurities on the surface of NMC811 induces the notably improved electrochemical performance, including higher capacity and Coulombic efficiency, reduced voltage polarization, and enhanced lithium-ion diffusion coefficients in the initial charge-discharge cycle. More importantly, the cleaned surface is beneficial for NMC811 to bolstering the cycling stability and rate capability in two promising sulfide-based SSEs systems (LPSCl and LGPS). The underlying degradation mechanism of cathode interface is investigated by XPS and XANES analyses. The results indicate that residual lithium compounds are the catalyst for accelerating the oxidation of sulfide SSEs. As a result, the formed by-products lead to severe side-reactions between NMC811 and sulfide SSEs, therefore inducing the formation of an undesirable CEI layer and structural degradation of NMC811. In contrast, removal of residual lithium compounds helps to alleviate the oxidation of sulfide SSEs and limits the severe interfacial side-reactions, therefore boosting the electrochemical performance of NMC811 cathodes. These findings are observed in both LPSCl and LGPS-based ASSLIBs, providing a strong evidence to prove the origin of degradation at cathode interface. Different from the prevailing protection coating methods, which require the addition of a new interfacial layer to suppress the side-reactions, removing the origin of the side-reactions from the pristine materials without introducing new materials into the system is a facile and scalable strategy towards realizing the industrial application of high-performance ASSLIBs.

Declaration of Competing Interest

The authors declare that they have no known competing financial interests or personal relationships that could have appeared to influence the work reported in this paper.

Acknowledgments

beamlines at CLS, Dr. Qunfeng Xiao, Dr. Mohsen Shakouri, and Dr. Weifeng Chen.

Supplementary materials

Supplementary material associated with this article can be found, in the online version, at doi:10.1016/j.ensm.2020.12.003.

References

[1] S. Randau, D.A. Weber, O. Kötz, R. Koerver, P. Braun, A. Weber, E. Ivers-Tiffée, T. Adermann, J. Kulisch, W.G. Zeier, F.H. Richter, J. Janek, Nat. Energy 5 (2020) 259–270.
[2] R. Chen, Q. Li, X. Yu, L. Chen, H. Li, Chem. Rev. 120 (2019) 6820–6877.
[3] H. Li, Joule 3 (2019) 911–914.
[4] H.-J. Deiseroth, S.-T. Kong, H. Eckert, J. Vannahme, C. Reiner, T. Zaiß, M. Schlosser, Angew. Chem. Int. Ed. 47 (2008) 755–758.
[5] Y. Kato, S. Hori, T. Saito, K. Suzuki, M. Hirayama, A. Mitsui, M. Yonemura, H. Iba, R. Kanno, Nat. Energy 1 (2016) 16030.
[6] C. Yu, Y. Li, M. Willans, Y. Zhao, K.R. Adair, F. Zhao, W. Li, S. Deng, J. Liang, M.N. Banis, R. Li, H. Huang, L. Zhang, R. Yang, S. Lu, Y. Huang, X. Sun, Nano Energy 69 (2020) 104396.
[7] X. Li, J. Liang, X. Yang, K.R. Adair, C. Wang, F. Zhao, X. Sun, Energy Environ. Sci. 13 (2020) 1429.
[8] W. Li, E.M. Erickson, A. Manthiram, Nat. Energy. 5 (2020) 26–34.
[9] S.-T. Myung, F. Maglia, K.-J. Park, C.S. Yoon, P. Lamp, S.-J. Kim, Y.-K. Sun, ACS Energy Lett. 2 (2017) 196–223.
[10] T. Li, X.-Z. Yuan, L. Zhang, D. Song, K. Shi, C. Bock, Electrochem. Energy Rev. 3 (2020) 43–80.
[11] Y. Zhu, X. He, Y. Mo, ACS Appl. Mater. Interfaces 7 (2015) 23685–23693.
[12] W. Zhang, D.A. Weber, H. Weigand, T. Arlt, I. Manke, D. Schröder, R. Koerver, T. Leichtweiss, P. Hartmann, W.G. Zeier, ACS Appl. Mater. Interfaces 9 (2017) 17835–17845.
[13] X. Li, Z. Ren, M. Norouzi Banis, S. Deng, Y. Zhao, Q. Sun, C. Wang, X. Yang, W. Li, J. Liang, X. Li, Y. Sun, K. Adair, R. Li, Y. Hu, T.-K. Sham, H. Huang, L. Zhang, S. Lu, J. Luo, X. Sun, ACS Energy Lett. 4 (2019) 2480–2488.
[14] S.P. Culver, R. Koerver, W.G. Zeier, J. Janek, Adv. Energy Mater. 9 (2019) 1900626.
[15] D. Cao, Y. Zhang, A.M. Nolan, X. Sun, C. Liu, J. Sheng, Y. Mo, Y. Wang, H. Zhu, Nano Lett. 20 (2020) 1483.
[16] A.Y. Kim, F. Strauss, T. Bartsch, J.H. Teo, T. Hatsukade, A. Mazilkin, J. Janek, P. Hartmann, T. Brezesinski, Chem. Mater. 31 (2019) 9664–9672.
[17] S. Deng, X. Li, Z. Ren, W. Li, J. Luo, J. Liang, J. Liang, M.N. Banis, M. Li, Y. Zhao, X. Li, C. Wang, Y. Sun, Q. Sun, R. Li, Y. Hu, H. Huang, L. Zhang, S. Lu, J. Luo, X. Sun, Energy Storage Mater. 27 (2020) 117–123.
[18] X. Li, L. Jin, D. Song, H. Zhang, X. Shi, Z. Wang, L. Zhang, L. Zhu, J. Energy Chem. 40 (2020) 39–45.
[19] X. Li, Q. Sun, Z. Wang, D. Song, H. Zhang, X. Shi, C. Li, L. Zhang, L. Zhu, J. Power Sources 456 (2020) 227997.
[20] S.W. Park, G. Oh, J.-W. Park, Y.-C. Ha, S.-M. Lee, S.Y. Yoon, B.G. Kim, Small 15 (2019) 1900235.
[21] T. Bartsch, F. Strauss, T. Hatsukade, A. Schiele, A.Y. Kim, P. Hartmann, J. Janek, T. Brezesinski, ACS Energy Lett. 3 (2018) 2539–2543.
[22] F. Walther, R. Koerver, T. Fuchs, S. Ohno, J. Sann, M. Rohnke, W.G. Zeier, J. Janek, Chem. Mater. 31 (2019) 3745–3755.
[23] H. Visbal, S. Fujiki, Y. Aihara, T. Watanabe, Y. Park, S. Doo, J. Power Sources 269 (2014) 396–402.
[24] H. Liu, Y. Yang, J. Zhang, J. Power Sources 162 (2006) 644–650.
[25] B. Wang, Y. Zhao, M.N. Banis, Q. Sun, K.R. Adair, R. Li, T.-K. Sham, X. Sun, ACS Appl. Mater. Interfaces 10 (2018) 1654–1661.
[26] J. Zheng, W. Shi, M. Gu, J. Xiao, P. Zuo, C. Wang, J.-G. Zhang, J. Electrochem. Soc. 160 (2013) A2212–A2219.
[27] X. He, X. Xu, L. Wang, C. Du, X. Cheng, P. Zuo, Y. Ma, G. Yin, J. Electrochem. Soc. 166 (2019) A143–A150.
[28] Y. Bi, W. Yang, R. Du, J. Zhou, M. Liu, Y. Liu, D. Wang, J. Power Sources 283 (2015) 211–218.
[29] R. Jung, R. Morasch, P. Karayaylali, K. Phillips, F. Maglia, C. Stinner, Y. Shao-Horn, H.A. Gasteiger, J. Electrochem. Soc. 165 (2018) A132–A141.
[30] C. Tian, D. Nordlund, H.L. Xin, Y. Xu, Y. Liu, D. Sokaras, F. Lin, M.M. Doeff, J. Electrochem. Soc. 165 (2018) A696–A704.
[31] J. Alvarado, C. Wei, D. Nordlund, T. Kroll, D. Sokaras, Y. Tian, Y. Liu, M.M. Doeff, Mater. Today 35 (2020) 87.
[32] M.E. Fleet, X. Liu, S.L. Harmer, H.W. Nesbitt, Can. Mineral. 43 (2005) 1589–1603.
[33] J. Prietzel, A. Botzaki, N. Tyufekchieva, M. Brettholle, J. Thieme, W. Klysubun, Environ. Sci. Tech. 45 (2011) 2878–2886.
[34] S. Deng, Y. Sun, X. Li, Z. Ren, J. Liang, K. Doyle-Davis, J. Liang, W. Li, M. Norouzi Banis, Q. Sun, R. Li, Y. Hu, H. Huang, L. Zhang, S. Lu, J. Luo, X. Sun, ACS Energy Lett. 5 (2020) 1243–1251.
[35] X. Yu, Y. Lyu, L. Gu, H. Wu, S.-M. Bak, Y. Zhou, K. Amine, S.N. Ehrlich, H. Li, K.-W. Nam, X.-Q. Yang, Adv. Energy Mater. 4 (2014) 1300950.
[36] E. Hu, X. Yu, R. Lin, X. Bi, J. Lu, S. Bak, K.-W. Nam, H.L. Xin, C. Jaye, D.A. Fischer, Nat. Energy 3 (2018) 690–698.
[37] P.-Y. Liao, J.-G. Duh, J.-F. Lee, J. Power Sources 189 (2009) 9–15.
[38] U.H. Kim, H.H. Ryu, J.H. Kim, R. Mücke, P. Kaghazchi, C.S. Yoon, Y.K. Sun, Adv. Energy Mater. 9 (2019) 1803902.
[39] X. Xu, H. Huo, J. Jian, L. Wang, H. Zhu, S. Xu, X. He, G. Yin, C. Du, X. Sun, Adv. Energy Mater. 9 (2019) 1803963.